



2H- and 1T- mixed phase few-layer MoS₂ as a superior to Pt co-catalyst coated on TiO₂ nanorod arrays for photocatalytic hydrogen evolution

Yunpeng Liu^{a,1}, Yuhang Li^{a,1}, Feng Peng^{a,b,*}, Yuan Lin^a, Siyuan Yang^c, Shengsen Zhang^c, Hongjuan Wang^a, Yonghai Cao^a, Hao Yu^a

^a School of Chemistry and Chemical Engineering, South China University of Technology, Guangzhou, Guangdong, 510640, China

^b School of Chemistry and Chemical Engineering, Guangzhou University, Guangzhou, 510006, China

^c College of Materials and Energy, South China Agricultural University, Guangzhou, 510642, China

ARTICLE INFO

Keywords:

Photocatalysis
Few-layer MoS₂
Hydrogen production
Photocatalytic mechanism
Electron transfer process

ABSTRACT

Recently, MoS₂ as an efficient co-catalyst has attracted much attention for photocatalytic water splitting. MoS₂ has two polymorphs: semiconducting phase (2H) and metallic phase (1T). The 2H- and 1T- MoS₂ show different reaction mechanism in photocatalytic H₂ evolution. However, so far, very few experiments have clearly evidenced the electron transfer process between TiO₂ and mixed phase MoS₂. This study for the first time has reported a simple hydrothermal synthesis method to prepare mixed phase few-layer MoS₂ nanosheets coated on TiO₂ nanorod arrays (MoS₂@TiO₂) with a conductive fluorine-doped tin oxide (FTO) as a substrate. The structure of mixed phase MoS₂ was characterized carefully. The designed MoS₂@TiO₂ exhibits two times higher activity than Pt@TiO₂ for photocatalytic H₂ evolution. The reliable conclusion that the photo-generated electrons from TiO₂ to MoS₂ nanosheets has clearly been evidenced by photoelectrochemical analyses and in-situ KPFM experiments, and the mixed phase MoS₂ here is a co-catalyst such like Pt rather than as a semiconductor. This study not only presents a series of solid experimental evidences to verify the electrons transfer process and photocatalytic mechanism, but also provides a new method in substituting MoS₂ for noble metal Pt as co-catalyst in high-efficiency photocatalytic water splitting into hydrogen.

1. Introduction

Semiconductor photocatalysis is one of the efficient strategies to solve energy crisis [1–3]. The solar conversion efficiency in photocatalytic H₂ production is primarily determined by the photoelectrode. The co-catalyst as active site can dramatically enhance the photoelectrode performance, due to its low activation potential for the H₂ evolution reaction and efficient separation of photo-generated charges [4]. Noble metals such as Ag, Pt, Pd and Au are outstanding co-catalysts in photocatalytic water splitting for H₂ evolution. But the high-cost and scarcity of noble metals have deadily restrained from their application of photocatalytic water splitting. Therefore, one widely used strategy for substituting the noble metals is to utilize the low-cost and abundant materials such as metal sulfides (NiS, WS₂, and MoS₂) [5–8]. Especially, MoS₂ has been applied to photocatalysis as an efficient co-catalyst due to its high-performance conductivity and good activity for the H₂ evolution [9]. As a two-dimensional (2D) layered material, the MoS₂ layers not only can conduct electrons like the graphene, but also can act

as the active sites of the H₂ evolution reaction [10]. This is because that there exist two kinds of phase of MoS₂, 2H semiconducting phase and 1T metallic phase. The 2H-MoS₂ can form semiconductor composites with other semiconductors, while the 1T-MoS₂ can only work as a co-catalyst like metal Pt. Previous studies have indicated that 1T-MoS₂ has higher efficient catalytic hydrogen activity than 2H-MoS₂, due to more active edge sites and low charge transfer resistance [11].

Most recently, Sang et al reported a kind of CdS/MoS₂/Mo sheets photocatalyst [12], the electrons from conduction band (CB) of CdS rapidly migrated to MoS₂ through Mo sheets for H₂ evolution reaction. It is proposed that photo-generated electron transfer between CdS and MoS₂ was caused by semiconductor heterostructure effect. Even if the MoS₂ here was 1T phase only as a metal co-catalyst, it was also regarded as an electrons acceptor. Therefore, the transfer direction of photo-generated electrons between CdS and MoS₂ was definite, as shown in Fig. S1a.

MoS₂ modified TiO₂ materials can significantly improve the photocatalytic performance [13–15]. However, the electron transfer

* Corresponding author at: School of Chemistry and Chemical Engineering, Guangzhou University, Guangdong, 510006, China.

E-mail address: fpeng@gzhu.edu.cn (F. Peng).

¹ Y.P. Liu and Y.H. Li contributed equally.

between mixed phase MoS₂ and TiO₂ were unidentified. It is all known that 2H-MoS₂ is a semiconductor with band gap from the bulk value of 1.2 eV to 1.8 eV for a single monolayer [16]. At the same time, 1T-MoS₂ has the characteristics of co-catalyst like metal Pt with the superior electrons conductivity and active sites for H₂ evolution. Yu reported the TiO₂/MoS₂/graphene composite photocatalyst which exhibited high photocatalytic H₂ evolution [10]. The electrons transfer path was assumed that the photo-generated electrons from the CB of TiO₂ transferred to MoS₂ nanosheets through the graphene for H₂ evolution. The MoS₂ here played a role as a co-catalyst to accept the electrons for H₂ evolution, which showed the characteristics of the metal. However, other studies have suggested that such MoS₂@TiO₂ system should be the heterojunction semiconductor photocatalyst, because the MoS₂ was commonly the 2H semiconducting phase. Due to the uncertain band gap of MoS₂, some researchers believed that the CB of fewer-layer MoS₂ should be more negative than that of TiO₂ [17]. Liu et al prepared N-TiO_{2-x}@MoS₂ heterojunction with a high photocatalytic activity, which was attributed to the transfer of photo-generated electrons from MoS₂ to TiO₂ [18]. The MoS₂ was considered as a semiconductor rather than a co-catalyst. If the electron transfer happened only in this way, the active sites for H₂ evolution should be in the TiO₂ instead of in the MoS₂, but TiO₂ self has a high overpotential and low activity for H₂ evolution. Therefore, it cannot help but suspect that there are some contradictions for this photocatalytic mechanism. Unlike the single phase MoS₂, the mixed phase MoS₂ with TiO₂ photocatalyst has a more complex situation for photocatalytic H₂ evolution. If the mixed phase MoS₂ is used as semiconductor (2H phase), the photo-generated electrons should transfer to TiO₂ from the CB of MoS₂ [19], as shown in S1b. On the contrary, if the mixed phase MoS₂ takes effect as co-catalyst (1T phase), the photo-generated electrons from CB of TiO₂ should transfer to mixed phase MoS₂, which is the active sites for H₂ evolution, as shown in Fig. S1c. Thus, there is no unified explanation and exact conclusion about the electron transfer between mixed phase MoS₂ and TiO₂. So far, very few experiments have clearly evidenced the electron transfer process between TiO₂ and mixed phase MoS₂.

This study aims to prepare highly active MoS₂ substituting for noble-metal Pt for photocatalytic H₂ evolution, and clearly certify electron transfer process between the TiO₂ and MoS₂. Herein, vertically standing few-layer and mixed phase MoS₂ nanosheets modified TiO₂ nanorod arrays (NRs) on FTO substrate were conveniently prepared by a simple hydrothermal method using highly dispersed MoO₃ as a precursor. The prepared MoS₂@TiO₂ NRs exhibited almost two times higher H₂ evolution rate of Pt@TiO₂ NRs. The mixed phase MoS₂ apparently showed the characteristic of 1T-MoS₂ like Pt, a series of solid experimental evidences have proven the photo-generated electron transfer process and photocatalytic mechanism.

2. Experimental section

2.1. Preparation of TiO₂ NRs

TiO₂ NRs on FTO were prepared by a reported hydrothermal method [20]. At first, 15 ml deionized water was mixed with 15 ml concentrated hydrochloric acid (36.5% by weight), and the solution was stirred for 5 min in the Teflon-lined stainless-steel autoclave (100 mL). After that, 450 μ L titanium butoxide (99% Aladdin) was added to the solution with strongly stirring for 10 min. The well-cleaned FTO substrates (5 \times 3 cm²) were placed into the Teflon-liner at an angle against the wall with the conducting side facing down. The hydrothermal synthesis was conducted at 170 °C for 7 h. The resultant sample was taken out, and rinsed extensively with deionized water, then dried at 60 °C for 1 h. After that, the sample was put into a muffle furnace under 450 °C for 1 h with a heating rate of 5 °C/min.

2.2. Fabrication of mixed phase MoS₂ nanosheets@TiO₂ NRs (MoS₂@TiO₂)

Mixed phase MoS₂ nanosheets were supported controllably on TiO₂ NRs (FTO) by a facile hydrothermal reaction. First, 35 mg MoO₃ powder (99%, Energy Chemical) and 100 mg potassium thiocyanate (KSCN 99.99%, Aladdin) were put in 30 ml deionized water with magnetic stirring for 1 h, and then subjected to high intensity ultrasonic treatment for 1 h to achieve highly dispersed MoO₃. After that, mixed solution was stirred for 5 min in the 100 ml Teflon-lined stainless-steel autoclave. The prepared TiO₂ NRs were placed into the Teflon-liner at an angle against the wall with the TiO₂ NRs side facing down. The hydrothermal synthesis was carried out at 200 °C for 6 h, 12 h, 18 h and 24 h respectively. The resultant samples were taken out and rinsed with deionized water, and then dried at 60 °C for 1 h. The resultant samples were labeled as MoS₂@TiO₂ (6 h), MoS₂@TiO₂ (12 h), MoS₂@TiO₂ (18 h), MoS₂@TiO₂ (24 h), respectively.

2.3. Fabrication of Pt@TiO₂

As the referential sample, Pt@TiO₂ was prepared by the simple photo-deposition method. A piece of TiO₂ NRs (FTO) was put into a Petri dish with 30 ml deionized water, and then H₂PtCl₆ aqueous solution (0.01 M) was added dropwise under stirring. Finally, they were irradiated under a 300 W Xe lamp for 20 min. Fig. S2 shows the photocatalytic H₂ evolution rate of Pt@TiO₂ with different loading content of Pt co-catalyst. It was found that when H₂PtCl₆ aqueous solution (0.01 M) of 400 μ L was added, the Pt@TiO₂ showed the highest photocatalytic H₂ evolution rate. Therefore, this optimal Pt@TiO₂ photocatalyst was used to compare with the MoS₂@TiO₂.

2.4. Characterizations

The morphologies and microstructures of these photocatalysts were characterized on field-emission scanning electron microscope (FESEM, Philips FEI Quanta 200 FEG) and transmission electron microscope (TEM, JEOL, JEM-2100 F). Atomic Force Microscopy (AFM) and Kelvin Probe Force Microscopy (KPFM) with additional illuminant (without infrared light) are used to obtain the structure imaging and surface potential (Bruker, Dimension ICON). The surface chemical states of photocatalysts were analyzed by X-ray photoelectron spectroscopy (XPS) on Kratos Axis Ultra DLD with Al K α X-ray. The banding energies of Mo, S, O, and Ti were referred to the C 1s peak at 284.8 eV. The crystal phases of samples were tested by X-ray powder diffractometer (XRD, Bruker D8 Advance) with Cu K α radiation source. The ultraviolet photoelectron spectrometer (UPS) were measured with a monochromatic He I light source (21.2 eV) and a VG Scienta R4000 analyzer. A bias of -5 V was applied to observe the secondary electron cutoff (SEC). The work function (ϕ) was determined by the difference between the photon energy and the binding energy of the secondary electron cutoff edge. Raman spectra of the prepared samples were recorded on LabRAM Aramis (HORIBA Jobin Yvon S.A.S.). The optical absorption properties of samples were performed by using a UV-vis diffuse reflectance spectroscope (DRS, U3010, Hitachi). Photoluminescence (PL) was collected on Hitachi F-7000 fluorescence spectrophotometer with the excitation wavelength of 320 nm. PL decay processes were recorded with Edinburgh Instruments FLS920 at room temperature (25 °C) with monitoring emission at 300 nm, and PL decay curves were fitted well by decay curves of ExpDec3 function: $A(t) = A_1 \exp(-t/\tau_1) + A_2 \exp(-t/\tau_2) + A_3 \exp(-t/\tau_3)$. And the average lifetimes were calculated by: $\tau_a = (A_1\tau_1^2 + A_2\tau_2^2 + A_3\tau_3^2) / (A_1\tau_1 + A_2\tau_2 + A_3\tau_3)$.

Photoelectrochemical measurements of the as-prepared samples were performed by an electrochemical workstation (CHI 760) with a three-electrode system, Ag/AgCl saturated KCl as a reference electrode, and platinum foil as a counter electrode. The illuminated area of the working electrode was about 9.0 cm². All the photoelectrochemical

measurements were carried out in 0.35 M Na₂S and 0.25 M Na₂SO₃ mixed aqueous solution electrolyte, which was irradiated by simulated solar light (PLS-SXE, 300 W Xe lamp).

2.5. Photocatalytic hydrogen evolution test

The photocatalytic H₂ evolution of all the samples were carried out in a closed gas-circulating CEL-SPH2N photocatalytic H₂ evolution system (Au-Light, China). A piece of the photocatalyst (FTO substrate, the effective area of 3 × 3 cm²) was immersed in 150 ml mixed aqueous solution of 0.35 M Na₂S and 0.25 M Na₂SO₃ with magnetic stirring. Photocatalytic reaction was carried out using a 300 W Xe lamp as the light source under vacuum environment of less than -0.09 Mpa. And the sample is 14 cm far away from the light source. Hydrogen generated was collected and analyzed by Fuli GC-9790 on-line gas chromatograph that was connected with a circulation line and equipped with a TCD detector.

3. Results and discussion

3.1. Material structure analyses

Fig. 1 shows the innovative preparation process of mixed phase MoS₂@TiO₂. The TiO₂ NRs first grew on FTO, and then the few-layer MoS₂ nanosheets were loaded on TiO₂ NRs by one-step hydrothermal method using highly dispersed MoO₃. The morphologies of the samples prepared in different hydrothermal times are shown in Fig. 2. As shown in Fig. 2a, the TiO₂ nanorods regularly grew on FTO substrate in the form of cuboid. For MoS₂@TiO₂ (6 h), the thin MoS₂ layers have coated the TiO₂ nanorod, which was the early growth stage of MoS₂ nanosheets, as shown in Fig. 2b. When the hydrothermal time extended to 12 h, the vertically standing and few-layer MoS₂ nanosheets have been shaped and grew well-distributed on TiO₂, as shown in Fig. 2c. MoS₂ nanosheets were coated uniformly on the top of TiO₂ nanorod exposing rich active edge sites for H₂ evolution reaction [21]. Fig. 2d exhibits that TiO₂ nanorods were completely coated by MoS₂ nanosheets when the hydrothermal time was 18 h. The cross-section view of MoS₂@TiO₂ (18 h) in Fig. 2e also shows that the MoS₂ nanosheets were assuredly distributed on the all outside surface of TiO₂ nanorod. Further increasing hydrothermal time, the MoS₂ nanosheets continued to grow into a hierarchical flowerlike structure with lots of petals and cover the TiO₂ nanorods, causing that the TiO₂ nanorods are hard to be observed, as shown in Fig. 2f. It was reported that the layer number of MoS₂ nanosheets significantly affected the photocatalytic performance [22–24], the few-layer MoS₂ nanosheets possessed maximum exposed edge sites and excellent ability of electron conduction. Here, the growth of MoS₂ nanosheets was inhibited by highly dispersed MoO₃. As shown in Fig. S3, if using the undispersed MoO₃ as a precursor, the MoS₂ nanosheets will reunite and be thicker.

XRD patterns of the prepared samples in different hydrothermal times are displayed in Fig. S4, except for the diffraction peaks of FTO substrate, it can be observed that the TiO₂ NRs consist of rutile crystal

phase with characteristic peaks at 2θ = 36° (101), 41.2° (111), 54.3° (211) and 62.7° (002) [25]. However, there are no extra characteristic diffraction peaks of MoS₂ for MoS₂@TiO₂ (6–18 h) samples, indicating that the MoS₂ nanosheets are fewer-layered [26]. For MoS₂@TiO₂ (24 h), the diffraction peak of MoS₂ at 14.1° (002) appears, because the multiple layered MoS₂ nanoflowers were aggregate on the TiO₂ nanorods (Fig. 2f).

TEM images of MoS₂@TiO₂ (12 h) are shown in Fig. 3, it is very clear that the MoS₂ nanosheets uniformly disperse on the surface of the TiO₂ nanorods (Figs. 3a–b) and there exists compact interface between the MoS₂ and TiO₂ (Figs. 3c–d). Fig. 3d further illustrates that the MoS₂ thin nanosheet is really standing vertically and exposes lot of active edge sites. The lattice spacings of 0.62 nm and 0.32 nm are attributed to (002) plane of MoS₂ and (110) plane of rutile TiO₂, respectively [27]. The EDX element mappings of the sample are shown in Fig. 3e and Fig. S5, the Mo, S, Ti and O elements are distributed accordantly within the selected area. The TEM images of MoS₂@TiO₂ (6, 18 and 24 h) are also shown in Fig. S6. With the hydrothermal time increasing, the content of MoS₂ nanosheets gradually increased and TiO₂ nanorods were finally completely coated by MoS₂ nanosheets, which are similar to the results of SEM.

With the reduction of the MoS₂ nanosheets thickness (number of layers), the two vibration modes of E_{2g}¹ and A_{1g} in Raman spectroscopy are shifted in the direction close to each other [28], and the number of layers of MoS₂ nanosheets can be determined by measuring the spacing of the two vibration modes [29]. As shown in Fig. 4a, the spacings of these two vibration modes for MoS₂@TiO₂ (12 and 18 h) samples are the same about 25.14 cm⁻¹, which indicates that the layers of MoS₂ did not thicken during the hydrothermal time from 12 h to 18 h, although the content of MoS₂ on TiO₂ nanorods increased [30]. For MoS₂@TiO₂ (24 h), the spacing is 26.46 cm⁻¹, indicating that the MoS₂ nanosheets aggregated and thickened on the TiO₂ nanorods when hydrothermal time extended to 24 h.

In order to accurately differentiate the phases of MoS₂, XPS was used to analyze the 1T and 2H phase of mixed phase MoS₂, as shown in Fig. 4. The full-scale XPS pattern of MoS₂@TiO₂ (6 h) shown in Fig. 4b reveals that Ti, O, S, Mo are the predominant elements. Previous studies have reported that the Mo 3d peaks of 1T-MoS₂ shifted to higher binding energies (about 1 eV), compared to the corresponding peaks of 2H-MoS₂, and the similar shifts also happened for the S 2p peaks of 1T-MoS₂ and 2H-MoS₂ [31]. The Mo 3d XPS spectrum presents Mo⁴⁺ as a dominated form, as shown in Fig. 4c. The binding energies at 229.0 eV for 3d_{5/2} and at 232.2 eV for 3d_{3/2} are ascribed to 2H-MoS₂, and at 230.2 eV for 3d_{5/2} and at 233.1 eV for 3d_{3/2} are ascribed to 1T-MoS₂ [32]. A pair peaks attributing to Mo⁶⁺ at 236.0 eV for Mo 3d_{3/2} and 234.3 eV for Mo 3d_{5/2} are observed, which come from MoO₃ [33,34]. A clear S 2s peak at 226.9 eV can also be observed. The S 2p peak with two doublets are shown in Fig. 4d, the binding energies at 163.3 eV for 2p_{1/2} and at 161.6 eV for 2p_{3/2} are attributed to 2H-MoS₂ [35]. Furthermore, the binding energies at 164.2 eV for 2p_{1/2} and at 162.4 eV for 2p_{3/2} is ascribed to bridging disulfides in 1T-MoS₂. The XPS for MoS₂@TiO₂ (18 h) sample are shown in Fig. S7. The peaks of 2H-MoS₂

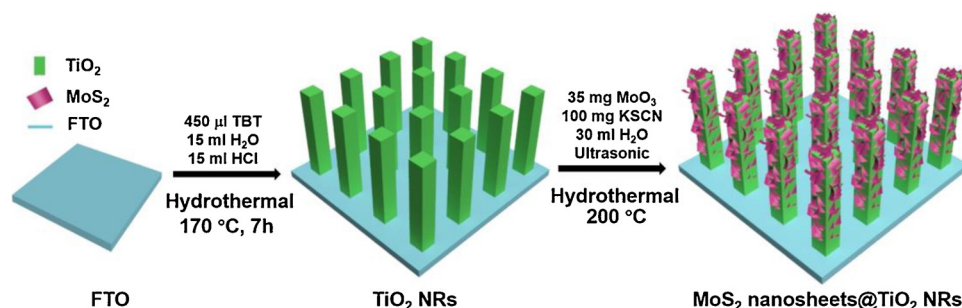


Fig. 1. Illustration of the preparation of MoS₂@TiO₂ (FTO).

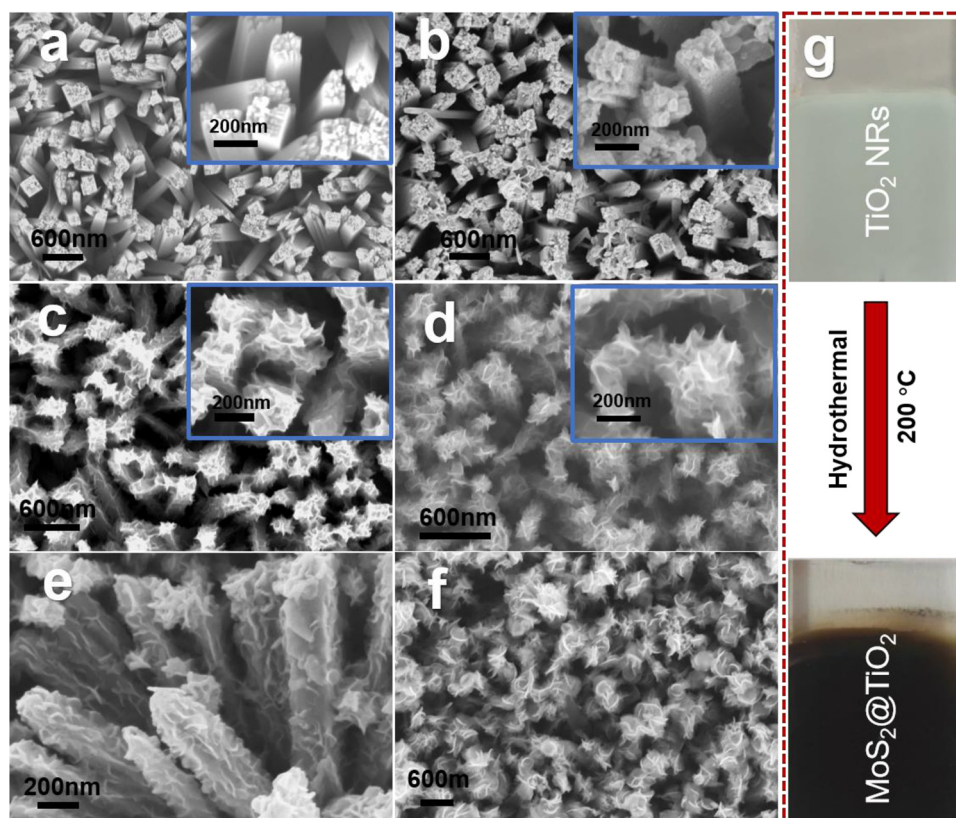


Fig. 2. SEM images of (a) TiO_2 NRAs, (b) $\text{MoS}_2@\text{TiO}_2$ (6 h), (c) $\text{MoS}_2@\text{TiO}_2$ (12 h), (d) $\text{MoS}_2@\text{TiO}_2$ (18 h), (e) cross-section view of $\text{MoS}_2@\text{TiO}_2$ (18 h) and (f) $\text{MoS}_2@\text{TiO}_2$ (24 h), and (g) the digital photos of the prepared TiO_2 NRAs and $\text{MoS}_2@\text{TiO}_2$ (18 h). The insets in (a–d) are the top views at high magnifications.

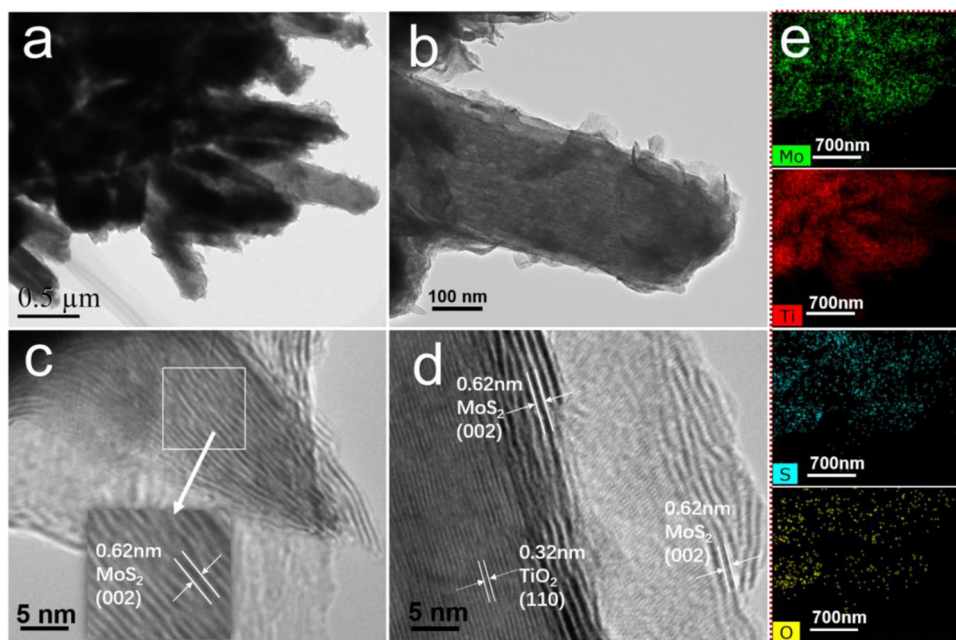


Fig. 3. (a, b) TEM and (c, d) HR-TEM images and (e) EDX element mapping of $\text{MoS}_2@\text{TiO}_2$ (12 h).

and 1 T- MoS_2 are also observed in Mo 3d spectrum. However, the peak of Mo $3d_{3/2}$ at 236.0 eV for Mo^{6+} almost disappeared, which means that almost all the MoO_3 were changed into 1 T- MoS_2 and 2H- MoS_2 . Similarly, the peaks of 2H- MoS_2 and 1 T- MoS_2 are observed in S 2p spectrum. In Fig. 4e, the binding energies of Ti^{4+} 2 $p_{1/2}$ and Ti^{4+} 2 $p_{3/2}$ are 464.7 eV and 459.0 eV respectively. As shown in the Fig. 4f, the XPS spectrum of high-resolution O 1s owns four peaks, situated at 530.0 eV,

530.5 eV, 531.4 eV and 532.4 eV, corresponding to Ti-O-Ti bond, Ti-O-Mo bond, adsorbed water and hydroxyl groups [36]. The peak of Ti-O-Mo bond indicates that the strong chemical bonding between MoS_2 and TiO_2 really exists, which is beneficial to the electron transport between MoS_2 and TiO_2 . Raman spectrum of the mixed phase $\text{MoS}_2@\text{TiO}_2$ is also shown in Fig. S8.

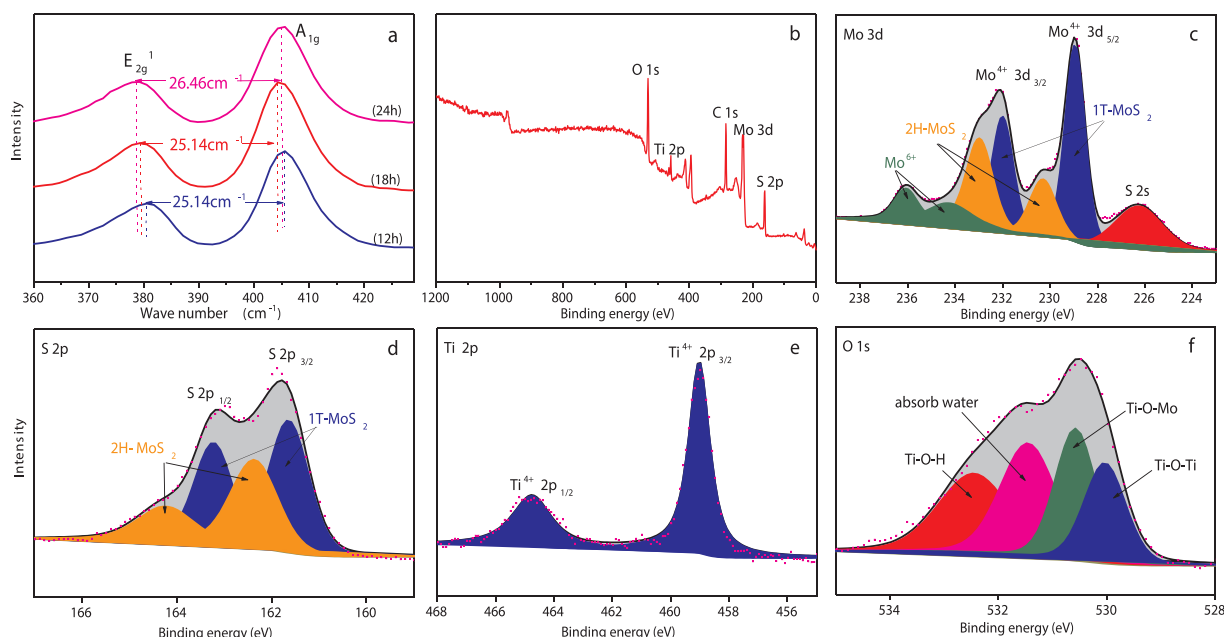


Fig. 4. Raman spectra (a) of MoS₂@TiO₂ (12 h), MoS₂@TiO₂ (18 h), MoS₂@TiO₂ (24 h) and XPS spectra of MoS₂@TiO₂ (6 h): (b) full-scale, (c) Mo 3d, (d) S 2p, (e) Ti 2p and (f) O 1 s.

3.2. Photocatalytic performances

UV–vis diffuse reflectance spectrum is used to analyze the optical properties of MoS₂@TiO₂ as shown in Fig. 5a. With the hydrothermal time increasing, the loading amount of MoS₂ also increased, which leads to the absorption in the visible light region (400–700 nm) increased because the black MoS₂ has strong optical absorption in the visible light region. For MoS₂@TiO₂ (24 h), an absorption peak is observed in about 650 nm which may be induced by the mixed phase MoS₂ nanoflowers on the TiO₂ nanorods.

The photocatalytic H₂ evolution under the simulated solar light was measured, as shown in Fig. 5b. The pure TiO₂ NRs shows a poor photocatalytic activity, which due to the high recombination rate of photo-generated electron-hole pairs. The photocatalytic performance for H₂ evolution obviously improves with the loading amount of MoS₂ increasing, the H₂ evolution rates of MoS₂@TiO₂ (6 h), MoS₂@TiO₂ (12 h) and MoS₂@TiO₂ (18 h) reach 3.87, 6.25 and 8.43 μmol cm^{−2} h^{−1}, which are 6.5, 10.3 and 13.8 times that of pure TiO₂ NRs respectively. When the loading amount of MoS₂ continues to increase, MoS₂ nanoflowers will cover the TiO₂ NRs as a shelter, which blocks the light to enter into the TiO₂ NRs. The photo-generated electrons largely reduce, therefore H₂ evolution rate of MoS₂@TiO₂ (24 h) decreases rapidly. Fig. 5c shows the recyclability of MoS₂@TiO₂ (18 h) for four cycles

lasting 20 h in total. The SEM images of Fig. S9 show the microstructures of MoS₂@TiO₂ (18 h) before and after photocatalytic reaction for 20 h. No significant structural changes are observed. However, the decline of hydrogen production rate is found after the cycle test, which is likely caused by slight exfoliation of MoS₂ nanosheets because of the hydrogen gas bubbles. In particular, a blank test in 0.35 M Na₂S and 0.25 M Na₂SO₃ mixed aqueous solution without photocatalyst was carried out under ultraviolet light irradiation, as shown in Fig. S10a. And background corrections of hydrogen production results in Fig. 5b and 5c were performed. Furthermore, the photocatalytic H₂ evolution rates of TiO₂ NRs and MoS₂@TiO₂ (18 h) in 20% methanol/water solutions are shown in Fig. S10b. The result indicates that the photocatalytic activity for H₂ evolution was also obviously improved after loading MoS₂.

The PL spectra in Fig. 6a show all the MoS₂@TiO₂ samples and Pt@TiO₂ are similar trend as pure TiO₂ NRs. They all have four peaks in ranges from 440 nm to 500 nm. The lowest emission intensity of MoS₂@TiO₂ indicates that MoS₂@TiO₂ has the lowest recombination of electron-hole pairs due to the efficient migration of charge carries between TiO₂ nanorods and MoS₂ nanosheets. These results also show the prepared MoS₂@TiO₂ catalysts are superior to the optimal Pt@TiO₂ for photo-generated charge migration. Fig. 6b shows the PL decay curves of the MoS₂@TiO₂ (18 h) and Pt@TiO₂, the results calculated are

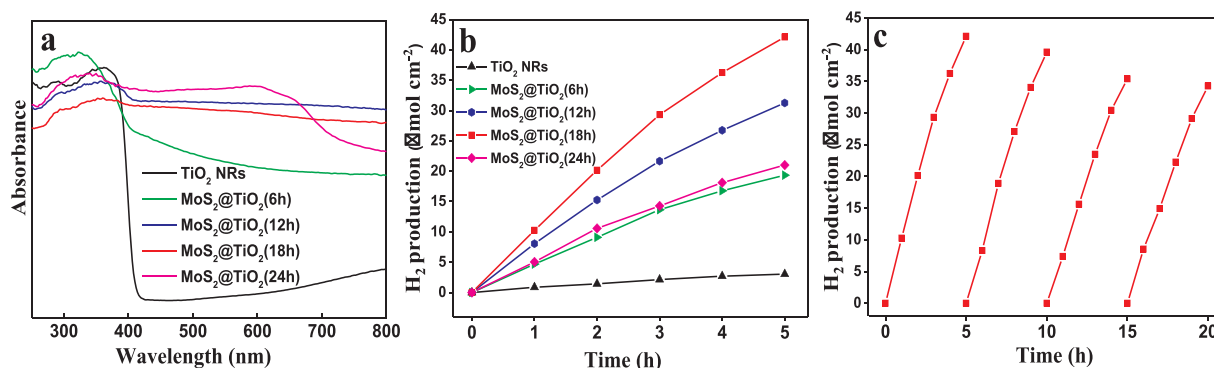


Fig. 5. (a) UV–vis diffuse reflectance spectra and (b) photocatalytic H₂ evolution curves of different samples, and (c) the recyclability test of MoS₂@TiO₂ (18 h) under 300 W Xe lamp.

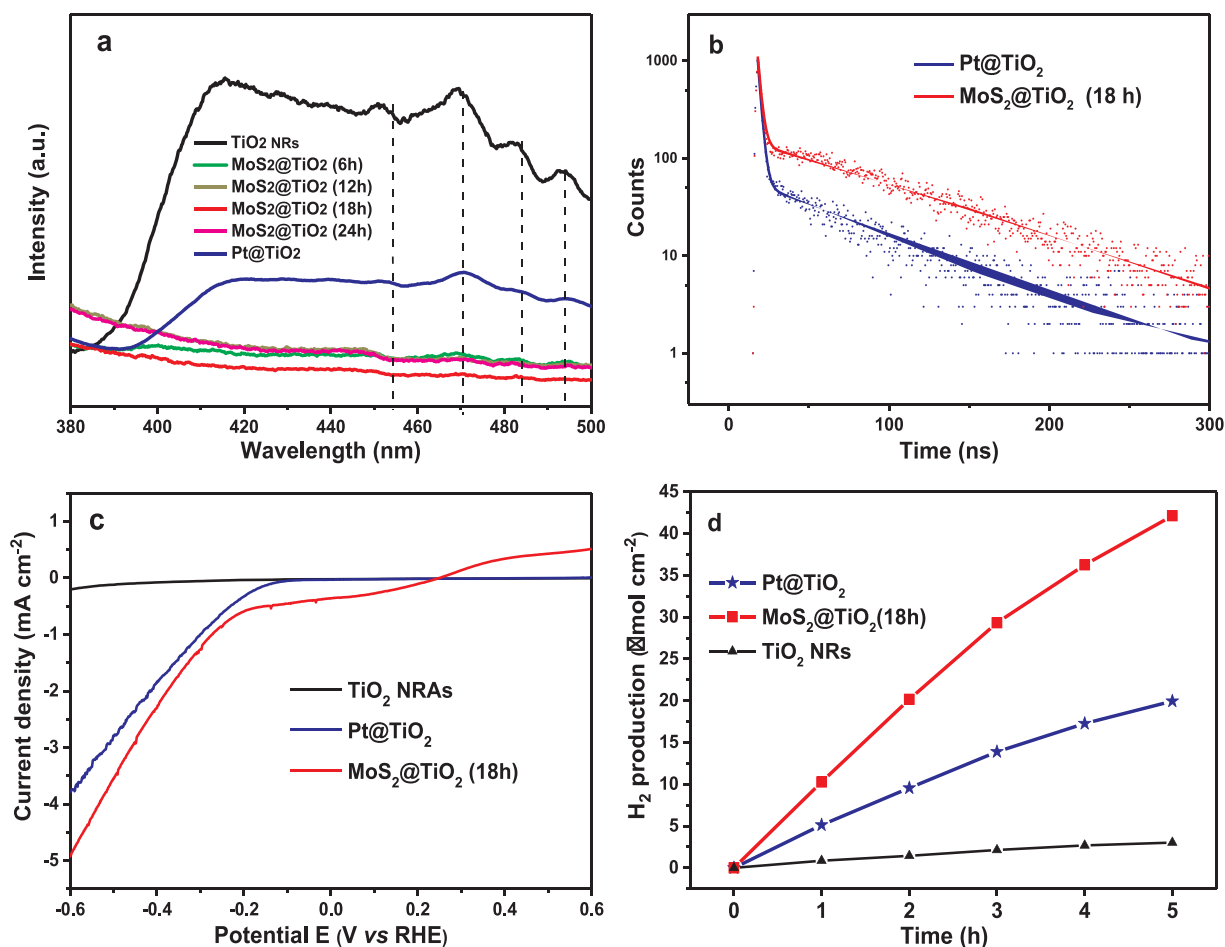


Fig. 6. (a) PL spectra, (b) time-resolved PL decay spectra, (c) HER polarization curves and (d) photocatalytic H₂ evolution under 300 W Xe lamp.

displayed in Table S1. The average PL decay time (τ_a) of Pt@TiO₂ is 2.18 ns, which is shorter than that of the MoS₂@TiO₂ (6.40 ns). The longer PL lifetime indicates lower nonradiative defect densities of MoS₂@TiO₂ than Pt@TiO₂ [37]. Furthermore, the contributions of MoS₂@TiO₂ and Pt@TiO₂ with fast decay times (τ_1 and τ_2), which are related to charge transfer, are almost the same (about 99%), showing that the interaction between the MoS₂ and TiO₂ is as strong as Pt and TiO₂ [38,39]. The results illustrate that the mixed phase MoS₂ shows the same characteristic with Pt. In order to reveal the characteristic of prepared MoS₂ like Pt, the HER (hydrogen evolution reaction) polarization [40] curves of TiO₂ NRs, Pt@TiO₂, and MoS₂@TiO₂ are shown in Fig. 6c. The HER overpotential of TiO₂ NRs is -0.42 V and the current density of HER is very low, indicating that pure TiO₂ NRs without co-catalyst is very difficult for hydrogen evolution. While MoS₂@TiO₂ exhibits a low overpotential of -0.15 V at a high current density of 0.49 mA cm⁻², which is derived from more active edge sites and superior conductivity. The result proves the electrons trapped by MoS₂ nanosheets are easier to react with H⁺ to produce H₂ just like the metal Pt [41]. It is worth noting that the current density of MoS₂@TiO₂ is higher than that of Pt@TiO₂. Fig. 6d shows that the H₂ evolution rate of MoS₂@TiO₂ is almost two times that of the Pt@TiO₂ NRs. This study indicates that the high active MoS₂ as co-catalyst is greatly promising to substitute for Pt for photocatalytic H₂ evolution. The HER polarization curves of MoS₂@TiO₂ (12 h) with scan rate from 5 mV to 50 mV was performed to further explore the hydrogen adsorption process between -0.2 and 0.2 V. As shown in Fig. S11, with the scan rate increasing, the peak of hydrogen adsorption between -0.2 and 0.2 V becomes more obvious [11,42]. It indicates that the ability to adsorb hydrogen of MoS₂ nanosheet is excellent, which is good for the hydrogen evolution

reaction.

3.3. Electron transfer mechanism

To evidence the transfer process of photo-generated electrons between TiO₂ and mixed phase MoS₂, an in-situ photo-deposition method experiment was designed. The TiO₂ NRs (FTO) and MoS₂@TiO₂ (FTO) were put into a Petri dish with 30 ml deionized water, 2 ml of H₂PtCl₆ aqueous solution (0.01 M) was added with stirring, and then irradiated under a 300 W Xe lamp for 5 min. The photo-generated electrons can directly reduce the Pt precursor into zero-valent Pt nanoparticles (NPs) on the surface of electron acceptor. It can be found more Pt NPs where there are more electrons. As shown in Fig. 7a and Fig. S12, for TiO₂ NRs without MoS₂ nanosheets, the many small Pt NPs can be clearly observed on the TiO₂ nanorods. When the mixed phase MoS₂ nanosheets existed, the Pt NPs with bigger size deposited on MoS₂ nanosheets, and few Pt NPs deposited on TiO₂ nanorods, as shown in Fig. 7b. It indicates that the photo-generated electrons in the conduction band of TiO₂ can easily transfer to the mixed phase MoS₂ nanosheets due to the intimate contact between metal phase 1T-MoS₂ and TiO₂ [43]. Fig. 7c is the corresponding AADF-STEM image of Pt@MoS₂@TiO₂ (18 h), almost all the bright spot (Pt) can be obviously seen in MoS₂ nanosheets. Fig. 7d is the corresponding elemental mapping images, the result shows that Pt particles are uniformly dispersed on the surface of MoS₂ nanosheets. In summary, the photo-generated electrons in TiO₂ transfer to MoS₂ nanosheets for photo-deposition reaction. Therefore, we believe that mixed phase MoS₂ in MoS₂@TiO₂ is the electrons acceptor and acts as active site of H₂ evolution such like Pt, meaning that the metal phase 1T-MoS₂ plays a leading role in mixed phase MoS₂ for the efficient

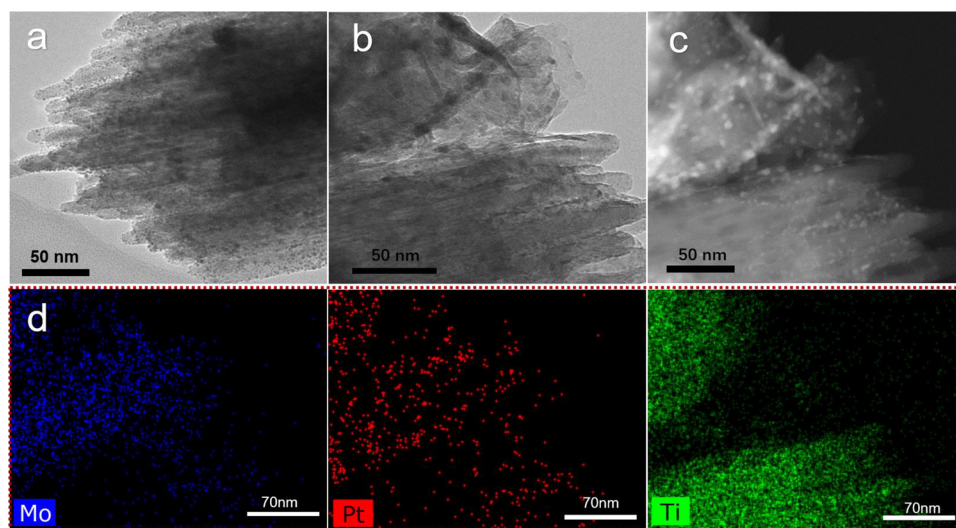


Fig. 7. TEM image of (a) Pt@TiO₂ NRAs and (b) Pt@MoS₂@TiO₂ (18 h), (c) HAADF-STEM image and (d) the corresponding elemental mapping images of Pt@MoS₂@TiO₂ (18 h).

charge separation.

In order to confirm that the transfer mechanism of photo-generated electrons is theoretically self-consistent, the work function (ϕ) was calculated by the difference between the photon energy (21.2 eV) and

the binding energy of the secondary cutoff edge in UPS [44]. As shown in Fig. 8a, for the TiO₂, the work function is 3.5 eV, and for mixed phase MoS₂, it is 4.5 eV. The smaller work function of TiO₂ indicates that it possesses a more negative Fermi level than MoS₂, hence, the electrons

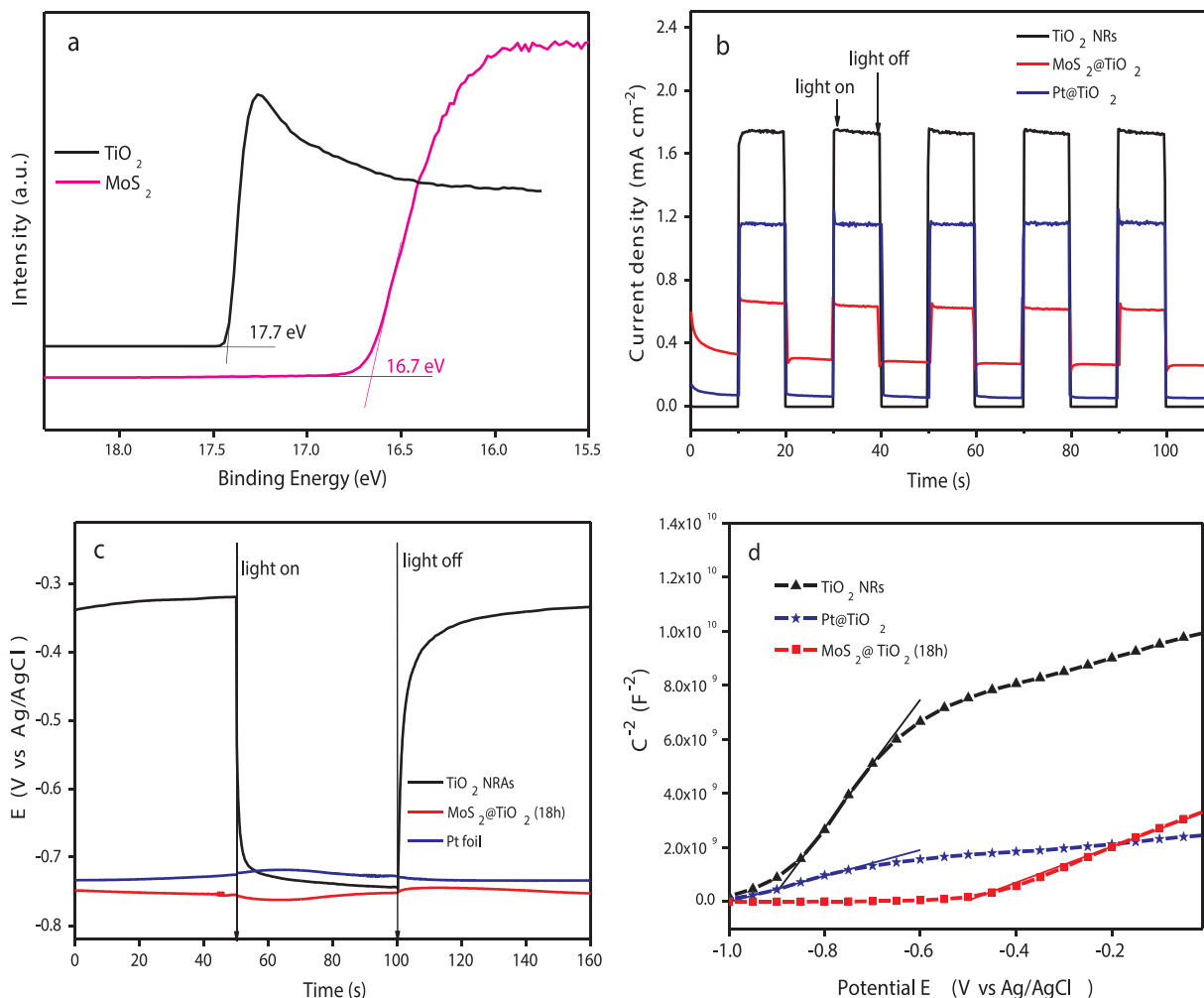


Fig. 8. (a) UPS spectra, (b) the transient photocurrent responses under 0 V vs Ag/AgCl (0.974 V vs RHE), (c) transient open-circuit voltage curves and (d) the Mott-Schottky plots acquired at 1000 Hz of samples.

are easy to transfer from TiO_2 to the mixed phase MoS_2 . In addition, to further confirm charge transfers between mixed phase MoS_2 and TiO_2 , the measurement of transient photocurrent response was carried out in aqueous solution, the test condition is same as that of photocatalytic H_2 evolution. If the charge transfer path assuredly conducts from TiO_2 to mixed phase MoS_2 , it can be supposed that the photo-generated electrons transfer to MoS_2 very fast, and then transfer to the electrolyte rapidly, which induces that few electrons transfer to FTO. It means that there are few electrons through the electrochemical workstation, so that the photocurrent response is weaker. When without the MoS_2 nanosheets, the photo-generated electrons from the TiO_2 transfer to the Pt electrode through the workstation. As is expected, the photocurrent of $\text{MoS}_2/\text{TiO}_2$ is far lower than that TiO_2 NRs, as shown in Fig. 8b. It is clearly evidenced that the photo-generated electrons of TiO_2 transfer to MoS_2 nanosheet and be captured, rather than transfer to FTO [45]. Fig. S13 shows the schematic illustration of the photocurrent response process of $\text{MoS}_2/\text{TiO}_2$ and TiO_2 . This mechanism is suitable for Pt/TiO_2 catalyst, whose photocurrent is also weaker than that of TiO_2 NRs, as shown Fig. 8b. But its photocurrent is higher than that of $\text{MoS}_2/\text{TiO}_2$, predicting that $\text{MoS}_2/\text{TiO}_2$ is more active than Pt/TiO_2 for photocatalytic H_2 evolution due to the plentiful active edge sites of MoS_2 nanosheets. In fact, the PL spectrum and H_2 evolution rate further explain that the external photocurrent of $\text{MoS}_2/\text{TiO}_2$ must be weaker [46]. These results indicate that the mixed phase MoS_2 possesses a fast electron conduction capability such like Pt metal.

The transient open-circuit voltage curves for TiO_2 NRs, $\text{MoS}_2/\text{TiO}_2$ (18 h) and Pt foil are shown in Fig. 8c. The open-circuit voltage of TiO_2 NRs becomes more negative after the light on, because the electrons excited in CB has the higher energy. Unlike the semiconductor, when the metal is irradiated by light, the open-circuit voltage hardly changes due to the superposition of CB and valance band (VB). Therefore, the open-circuit voltage curve of Pt foil is relatively smooth after the light on. As expected, $\text{MoS}_2/\text{TiO}_2$ catalyst has a similar characteristic with Pt, it further proves that the mixed phase MoS_2 in $\text{MoS}_2/\text{TiO}_2$ photocatalyst plays a role as the electron conductor like metal rather than semiconductor. Fig. 8d shows Mott-Schottky plots for TiO_2 NRs, $\text{MoS}_2/\text{TiO}_2$ and Pt/TiO_2 . All the samples have a positive slope, suggesting that they are n-type semiconductor. Their carrier densities can be estimated by equation below [47,48].

$$N_d = (2/e_0\epsilon\epsilon_0) [d(1/C^2)/dV]^{-1}$$

Where N_d , e_0 , ϵ , ϵ_0 and $d(1/C^2)/dV$ represent the carrier density, electron charge, the dielectric coefficient (about 170), the permittivity of vacuum, the straight slope obtained from the plot. The carrier densities of TiO_2 NRs, Pt/TiO_2 and $\text{MoS}_2/\text{TiO}_2$ are calculated to be 3.50×10^{17} , 1.66×10^{18} and $1.24 \times 10^{18} \text{ cm}^{-3}$. The carrier density of $\text{MoS}_2/\text{TiO}_2$ is much larger than that of TiO_2 NRs, and close to that of Pt/TiO_2 . It can be concluded that the mixed phase MoS_2 is excellent co-catalyst like Pt due to the abundantly exposed active edge sites of MoS_2 nanosheets [49].

The flat band energies versus Ag/AgCl for TiO_2 , $\text{MoS}_2/\text{TiO}_2$ and Pt/TiO_2 are -0.91, -0.51 and -0.99 eV, respectively, which are obtained from the Mott-Schottky plots. Under the room temperature, the compensation potential about 0.025 eV vs. normal hydrogen electrode (NHE) should be considered. Therefore, the Fermi levels vs. NHE (EAg/AgCl is about 0.197 eV vs. NHE) of TiO_2 , Pt/TiO_2 and $\text{MoS}_2/\text{TiO}_2$ are calculated to be -0.69, -0.29 and -0.77 eV, respectively. The results are consistent with the UPS characterization. Because the TiO_2 has a more negative Fermi level than MoS_2 , after the TiO_2 is loaded with MoS_2 , the Fermi level of $\text{MoS}_2/\text{TiO}_2$ will be more positive than TiO_2 .

The in-situ KPFM with the additional illuminant is used to measure the change of surface potential of the $\text{MoS}_2/\text{TiO}_2$ NRs when the sample is excited by light, the detail of in-situ KPFM device is shown in Fig. S14. Fig. 9a shows the AFM image of the $\text{MoS}_2/\text{TiO}_2$ NRs, and the morphology of the sample is consistent with the result of SEM (Fig. 9c

top). The electrons transfer will cause the change of electron concentration in MoS_2 , leading to the potential differences measured by KPFM. The KPFM surface potential images before illumination (top) and in illumination (bottom) of the sample are shown in Fig. 9b. The deeper color of KPFM image after irradiated by light indicates the more negative potential regions. What more, all the line scans of the potential across the $\text{MoS}_2/\text{TiO}_2$ NRs prove that the surface potentials decline when the sample is excited by light (from about 300 mV to 100 mV), as shown in Fig. 9d. The declining negative potential is caused by more rich electron. The primary reason for a potential difference across the $\text{MoS}_2/\text{TiO}_2$ NRs is that electrons transfer from the TiO_2 to the surface MoS_2 [50,51]. Due to this charge transfer, an electrical potential difference is established within the NRs that is equal in magnitude to the vacuum level shift that is accompanied by the Fermi level alignment. The Fermi level drawing at nonequilibrium is shown in Fig. 9c. In these NRs, electrons are expected to be transferred from the TiO_2 to the MoS_2 due to the difference of Fermi level. The electrons transfer process is directly derived according to the in-situ KPFM.

Due to the existence of 2H- MoS_2 , the mixed phase MoS_2 should show the characteristic of the semiconductor. The VB of MoS_2 was measured by UPS, as shown in Fig. S15, the VB position of mixed phase MoS_2 is 1.1 eV [52,53]. The inset is the Tauc plots of mixed phase MoS_2 , which indicates that the band gap is 1.49 eV. So, the CB position of MoS_2 is -0.39 eV, which is more negative than TiO_2 . However, for $\text{MoS}_2/\text{TiO}_2$, no Pt NPs were detected in photo-deposition process with visible light (Fig. S16a). XPS spectrum of this sample is shown in Fig. S16b, no peaks of zero-valent Pt can be found. The mixed phase MoS_2 in this photocatalyst seemingly do not work as the semiconductor, otherwise the mixed phase MoS_2 with narrow band gap should be excited and reduced the Pt precursor into zero-valent Pt under visible light. The interesting phenomenon is explained that the semiconducting 2H- MoS_2 has been excited by visible light, but the photo-generated electron-hole pairs recombined too quickly to realize the photo-reduction reaction due to the narrow band gap of 2H- MoS_2 and the excellent conductivity of 1 T- MoS_2 . The mixed phase MoS_2 apparently shows the characteristic of 1 T- MoS_2 and the MoS_2 here is considered as the metal.

In order to further figure out why mixed phase MoS_2 acts as a co-catalyst such like Pt rather than as a semiconductor, the band structures of 2H- MoS_2 , 1 T- MoS_2 and mixed phase MoS_2 were assessed through Perdew-Burke-Ernzerh (PBE) exchange-correlation functional (see Supporting Information). The optimized bulk phase crystals of 2H- MoS_2 , 1 T- MoS_2 and mixed phase MoS_2 are shown in Fig. S17. The calculated band structures of 2H- MoS_2 and 1 T- MoS_2 represent a semiconductor and a conductor, respectively, as shown in Fig. 10. When the 2H- MoS_2 layer is intercalated into the lattice of 1 T- MoS_2 , the newly introduced energy band locates in the vicinity of the pristine gap, leading to a continuous band across the Fermi level. This result indicates that the mixed phase MoS_2 exhibits the conductor characteristic due to the intercalation of 1 T- MoS_2 layer, which is favorable for accepting the photo-generated electrons from TiO_2 to produce hydrogen. The PBE calculation of the mixed phase MoS_2 provides theoretical support for the above conclusions.

Based on the above analysis, a possible photocatalytic H_2 evolution mechanism of $\text{MoS}_2/\text{TiO}_2$ (FTO) are illustrated in Fig. 11. Under visible light illumination (Fig. 11a), TiO_2 cannot be excited, while 2H- MoS_2 can be excited, but the recombination of photo-generated electron-hole pairs rapidly happen in interior of 2H- MoS_2 or on the surface of 1 T- MoS_2 , because the 1 T- MoS_2 is a good electron receiver and it contacts so closely with 2H- MoS_2 . When under ultraviolet light illumination (Fig. 11b), TiO_2 is excited to generate electron-hole pairs, most of photo-generated electrons in CB of TiO_2 can immediately transfer to 1 T- MoS_2 due to the metal characteristic. As a photoelectron receiver, 1 T- MoS_2 acts as active sites for H_2 evolution [54]. Meanwhile, the photo-generated holes on VB of TiO_2 react with S^{2-} or SO_3^{2-} . This effective electron transport between TiO_2 and MoS_2 tremendously decreases the recombination of electron-hole pairs and prolong the

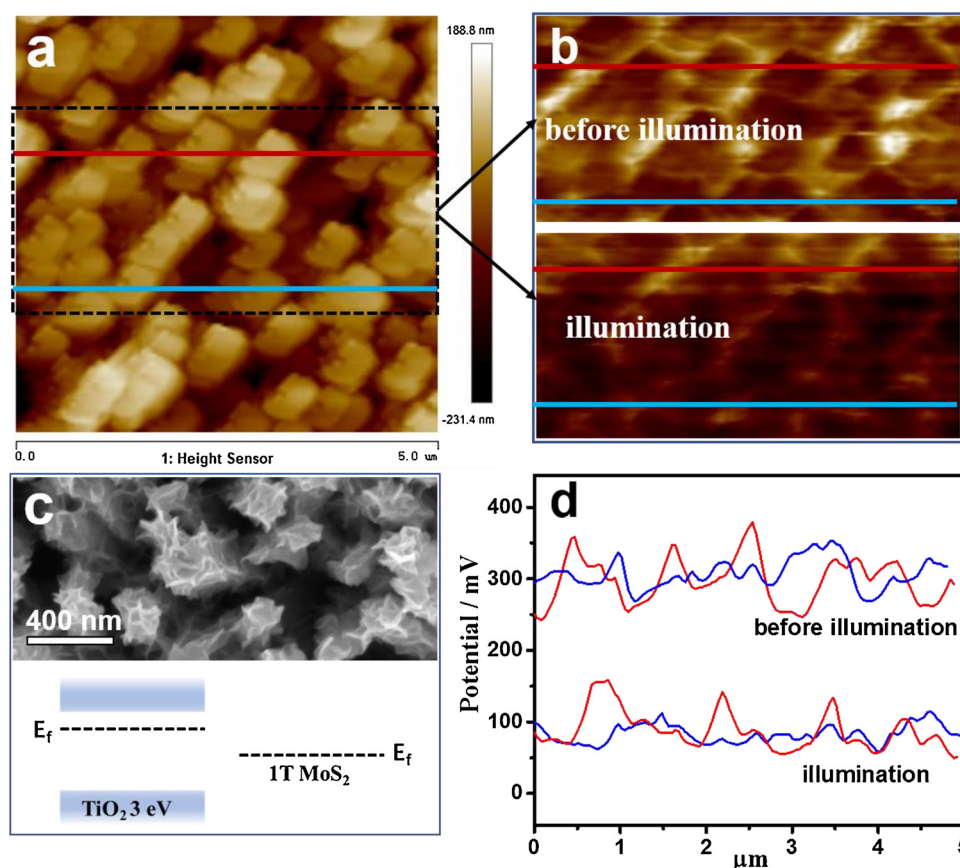


Fig. 9. (a) AFM image of $\text{MoS}_2/\text{TiO}_2$ NRs, (b) KPFM surface potential images corresponding to the part of dotted line in AFM image, (c) representative SEM image of $\text{MoS}_2/\text{TiO}_2$ NRs and nonequilibrium alignment energy levels of MoS_2 and TiO_2 , (d) line scans of the potential across the sample (red and blue line scans corresponding to the sites of red and blue lines in KPFM potential images). (For interpretation of the references to colour in this figure legend, the reader is referred to the web version of this article.)

charge life time. In addition, MoS_2 as a co-catalyst has a low HER overpotential, improving the hydrogen evolution.

4. Conclusions

In summary, the vertical and few-layer MoS_2 nanosheets coated on TiO_2 NRs/FTO were synthesized via simple hydrothermal method using highly dispersed MoO_3 as a precursor. Most importantly, 2H- and 1T-mixed phase few-layer MoS_2 nanosheets were prepared by this facile

method for the first time. The designed $\text{MoS}_2/\text{TiO}_2$ catalyst exhibits two times higher activity than Pt/TiO_2 for photocatalytic H_2 evolution due to the abundantly exposed active edge sites of MoS_2 nanosheets. This study indicates that the high active MoS_2 as co-catalyst is greatly promising to substitute for Pt for photocatalytic H_2 evolution.

The mixed phase MoS_2 apparently showed the characteristic of metal phase 1T- MoS_2 like Pt, which facilitated charge carrier separation and provided active sites for H_2 evolution. The photocatalytic mechanisms for the H_2 evolution and the electrons transfer process

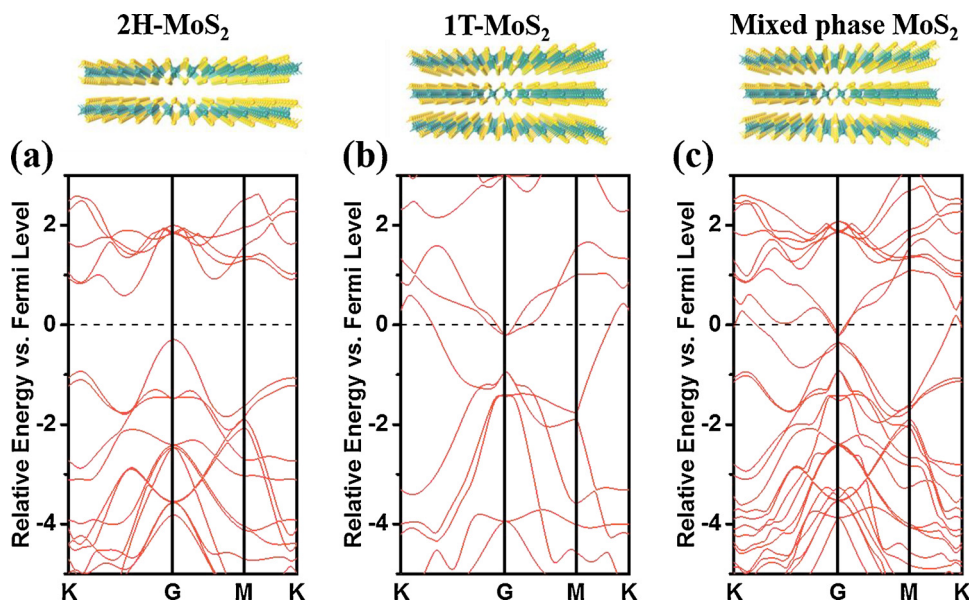


Fig. 10. PBE calculated band structures of 2H- MoS_2 (a), 1T- MoS_2 (b) and mixed phase MoS_2 (c).

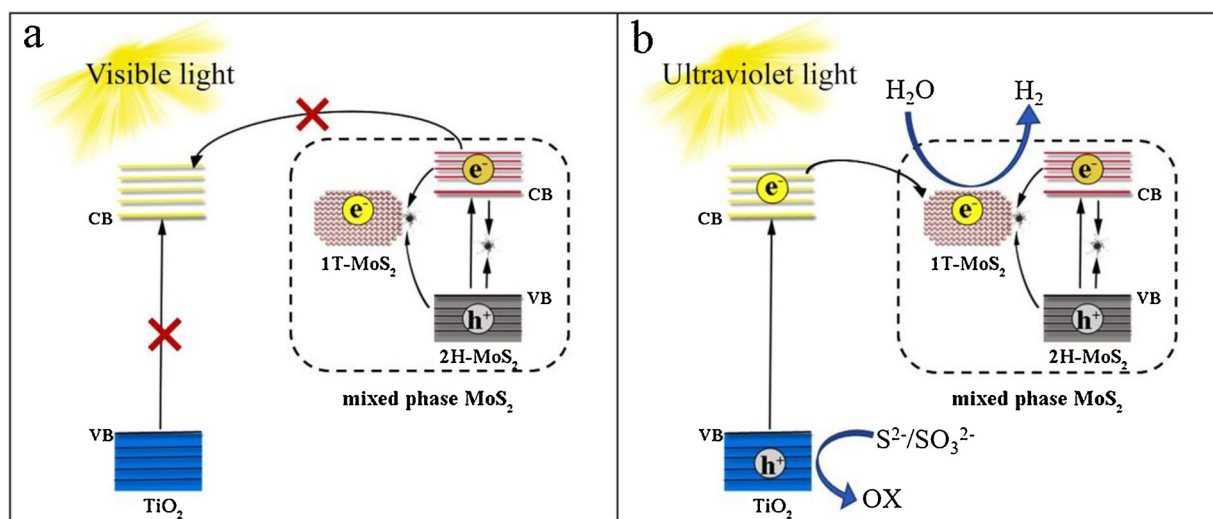


Fig. 11. The charge transfer process and photocatalytic H_2 evolution mechanism under visible light (a) and ultraviolet light (b).

were analyzed in detail. The results clearly have evidenced that photo-generated electrons of TiO_2 truly transfer to the MoS_2 nanosheets and the MoS_2 here is a co-catalyst such like Pt rather than as a semiconductor. The electrons transfer process from the TiO_2 to the MoS_2 is directly proven by in-situ KPFM experiment. This study not only presents a series of solid experimental evidences to obtain reliable conclusion about the electrons transfer mechanism between MoS_2 and TiO_2 , but also provides new method to prepare this non-noble metal monolithic photocatalyst for efficient photocatalytic H_2 production.

Acknowledgements

We acknowledge the financial support from the National Natural Science Foundation of China (No. 21673080), the Provincial Science and Technology Project of Guangdong (No. 2014A030312007) and the Fundamental Research Funds for the Central Universities (No. 2015ZP021).

Appendix A. Supplementary data

Supplementary material related to this article can be found, in the online version, at doi:<https://doi.org/10.1016/j.apcatb.2018.09.040>.

References

- [1] H. Huang, X. Han, X. Li, S. Wang, P.K. Chu, Y. Zhang, *ACS Appl. Mater. Interfaces* 7 (2015) 482–492.
- [2] H. Huang, K. Xiao, T. Zhang, F. Dong, Y. Zhang, *Appl. Catal. B: Environ.* 203 (2017) 879–888.
- [3] Y. Liu, S. Yang, S. Zhang, H. Wang, H. Yu, Y. Cao, F. Peng, *Int. J. Hydrogen Energy* 43 (2018) 5551–5560.
- [4] Y. Lin, S. Yang, Y. Liu, S. Zhang, H. Wang, H. Yu, F. Peng, *Int. J. Hydrogen Energy* 42 (2017) 19942–19950.
- [5] B. Han, Y.H. Hu, *Energy Sci. Eng.* 4 (2016) 285–304.
- [6] S. Iqbal, Z. Pan, K. Zhou, *Nanoscale* 9 (2017) 6638–6642.
- [7] W. Zhou, Z. Yin, Y. Du, X. Huang, Z. Zeng, Z. Fan, H. Liu, J. Wang, *Small* 9 (2013) 140–147.
- [8] X. Liu, X. Liang, P. Wang, B. Huang, X. Qin, X. Zhang, Y. Dai, *Appl. Catal. B: Environ.* 203 (2017) 282–288.
- [9] X. Zhang, Z. Lai, C. Tan, H. Zhang, *Angew. Chem. Int. Ed.* 55 (2016) 8816–8838.
- [10] X. Xiang, J. Yu, M. Jaroniec, *J. Am. Chem. Soc.* 134 (2012) 6575–6578.
- [11] Z.W. Seh, J. Kibsgaard, C.F. Dickens, I. Chorkendorff, J.K. Nørskov, T.F. Jaramillo, *Science* 355 (2017) 6321.
- [12] L. Zhao, J. Jia, Z. Yang, J. Yu, A. Wang, Y. Sang, W. Zhou, H. Liu, *Appl. Catal. B: Environ.* 210 (2017) 290–296.
- [13] L. Gomathi Devi, R. Kavitha, *Appl. Surf. Sci.* 360 (2016) 601–622.
- [14] S. Cravanzola, L. Muscuso, F. Cesano, G. Agostini, A. Damin, D. Scaranio, A. Zecchina, *Langmuir* 31 (2015) 5469–5478.
- [15] L. Guo, Z. Yang, K. Marcus, Z. Li, B. Luo, L. Zhou, X. Wang, Y. Du, Y. Yang, *Energy Environ. Sci.* 11 (2018) 106–114.

- [16] K.F. Mak, C. Lee, J. Hone, J. Shan, T.F. Heinz, *Phys. Rev. Lett.* 105 (2010) 136805.
- [17] X. Hai, W. Zhou, K. Chang, H. Pang, H. Liu, L. Shi, F. Ichihara, J. Ye, *J. Mater. Chem. A* 5 (2017) 8591–8598.
- [18] X. Liu, Z. Xing, Y. Zhang, Z. Li, X. Wu, S. Tan, X. Yu, Q. Zhu, W. Zhou, *Appl. Catal. B: Environ.* 201 (2017) 119–127.
- [19] D.A. Reddy, H. Park, S. Hong, D.P. Kumar, T.K. Kim, *J. Mater. Chem. A* 5 (2017) 6981–6991.
- [20] B. Liu, E.S. Aydil, *J. Am. Chem. Soc.* 131 (2009) 3985–3985.
- [21] J. Xie, H. Zhang, S. Li, R. Wang, X. Sun, M. Zhou, J. Zhou, X.W. Lou, Y. Xie, *Adv. Mater.* 25 (2013) 5807–5813.
- [22] C. Liu, L. Wang, Y. Tang, S. Luo, Y. Liu, S. Zhang, Y. Zeng, Y. Xu, *Appl. Catal. B: Environ.* 164 (2015) 1–9.
- [23] M. Shen, Z. Yan, L. Yang, P. Du, J. Zhang, B. Xiang, *Chem. Commun.* 50 (2014) 15447–1449.
- [24] D. Wang, Y. Xu, F. Sun, Q. Zhang, P. Wang, X. Wang, *Appl. Surf. Sci.* 377 (2016) 221–227.
- [25] Q. Zhang, Z. Hai, A. Jian, H. Xu, C. Xue, S. Sang, *Nanomaterials* 6 (2016) 138.
- [26] L. Wang, X. Liu, J. Luo, X. Duan, J. Crittenden, C. Liu, S. Zhang, Y. Pei, Y. Zeng, X. Duan, *Angew. Chem. Int. Ed.* 56 (2017) 7610–7614.
- [27] Y.-H. Tan, K. Yu, J.-Z. Li, H. Fu, Z.-Q. Zhu, *J. Appl. Phys.* 116 (2014) 064305.
- [28] C.N. Rao, H.S. Matte, U. Maitra, *Angew. Chem. Int. Ed.* 52 (2013) 13162–13185.
- [29] B.C. Windom, W.G. Sawyer, D.W. Hahn, *Tribol. Lett.* 42 (2011) 301–310.
- [30] H. Li, J. Wu, Z. Yin, H. Zhang, *Acc. Chem. Res.* 47 (2014) 1067–1075.
- [31] X. Geng, W. Sun, W. Wu, B. Chen, A. Al-Hilo, M. Benamara, H. Zhu, F. Watanabe, J. Cui, T.P. Chen, *Nat. Commun.* 7 (2016) 10672.
- [32] K. Chang, X. Hai, H. Pang, H. Zhang, L. Shi, G. Liu, H. Gao, M. Li, J. Ye, *Adv. Mater.* 28 (2016) 10033–10041.
- [33] H. Liu, T. Lv, C. Zhu, X. Su, Z. Zhu, *J. Mol. Catal. A: Chem.* 396 (2015) 136–142.
- [34] X. Zhou, M. Lickleder, P. Schmuki, *Electrochem. Commun.* 73 (2016) 33–37.
- [35] H. Vrubel, D. Merki, X. Hu, *Energy Environ. Sci.* 5 (2012) 6136–6144.
- [36] M. Sun, Y. Wang, Y. Fang, S. Sun, Z. Yu, *J. Alloys Compd.* 684 (2016) 335–341.
- [37] N. Yantara, S. Bhaumik, F. Yan, D. Sabba, H.A. Dewi, N. Mathews, P.P. Boix, H.V. Demir, S. Mhaisalkar, *J. Phys. Chem. Lett.* 6 (2015) 4360–4364.
- [38] S. Zhang, X. Wang, J. Hu, Z. Xie, H. Lei, F. Peng, *Electrochim. Acta* 252 (2017) 368–373.
- [39] S. Sun, D. Yuan, Y. Xu, A. Wang, Z. Deng, *ACS Nano* 10 (2016) 3648–3657.
- [40] Y. Li, H. Wang, L. Xie, Y. Liang, G. Hong, H. Dai, *J. Am. Chem. Soc.* 133 (2011) 7296–7299.
- [41] J. Guo, F. Li, Y. Sun, X. Zhang, L. Tang, *J. Power Sources* 291 (2015) 195–200.
- [42] B.E. Conway, B.V. Tilak, *Electrochim. Acta* 47 (2002) 3571–3594.
- [43] X. Song, G. Chen, L. Guan, H. Zhang, J. Tao, *Appl. Phys. Express* 9 (2016) 095801.
- [44] A. Wu, C. Tian, Y. Jiao, Q. Yan, G. Yang, H. Fu, *Appl. Catal. B: Environ.* 203 (2017) 955–963.
- [45] X. Yang, H. Li, W. Zhang, M. Sun, L. Li, N. Xu, J. Wu, J. Sun, *ACS Appl. Mater. Interfaces* 9 (2017) 658–667.
- [46] Y. Shen, X. Yu, W. Lin, Y. Zhu, Y. Zhang, *Appl. Surf. Sci.* 399 (2017) 67–76.
- [47] C.C. Wang, P.H. Chou, *Nanotechnology* 27 (2016) 325401.
- [48] K. Zhang, W. Zhou, L. Chi, X. Zhang, W. Hu, B. Jiang, K. Pan, G. Tian, Z. Jiang, *ChemSusChem* 9 (2016) 2841–2848.
- [49] Z. Yin, B. Chen, M. Bosman, X. Cao, J. Chen, B. Zheng, H. Zhang, *Small* 10 (2014) 3537–3543.
- [50] W. Melitz, J. Shen, A.C. Kummel, S. Lee, *Surf. Sci. Rep.* 66 (2011) 1–27.
- [51] S.U. Nanayakkara, G. Cohen, C.S. Jiang, M.J. Romero, K. Maturova, M. Al-Jassim, J. van de Lagemaat, Y. Rosenwaks, J.M. Luther, *Nano Lett.* 13 (2013) 1278–1284.
- [52] K. Xiao, Y. He, T. Zhang, F. Dong, X. Du, Y. Zhang, *Appl. Catal. B: Environ.* 199 (2016) 75–86.
- [53] H. Huang, Y. He, X. Du, P.K. Chu, Y. Zhang, *ACS Sustain. Chem. Eng.* 3 (2015) 3262–3273.
- [54] K. Zhou, Y. Zhu, X. Yang, X. Jiang, C. Li, *New J. Chem.* 35 (2011) 353–359.